TUTORIAL REVIEW

# Recent progress of integrated optics planar lightwave circuits

KATSUNARI OKAMOTO
*NTT Opto-electronics Laboratories 162 Tokai, Ibaraki, 319-11, Japan*

Planar lightwave circuits (PLCs) are waveguide devices that integrate fiber-matched optical waveguides on silicon or glass substrate to provide an efficient means of interaction for the guided-wave optical signals. PLCs provide various important and functional devices for optical wavelength division multiplexing (WDM), time division multiplexing (TDM) systems and subscriber networks. This paper reviews the recent progress and future prospects of PLC technologies including arrayed-waveguide grating multiplexers, optical add/drop multiplexers, programmable dispersion equalizers and hybrid optoelectronics integration technologies.

## 1. Introduction

The most prominent feature of the silica waveguides is their simple and well-defined waveguide structures [1]. This allows us to fabricate multi-beam or multi-stage interference devices such as arrayed-waveguide gratings and lattice-form programmable dispersion equalizers. A variety of passive PLCs such as $N \times N$ star couplers, $N \times N$ arrayed-waveguide grating multiplexers and thermo-optic matrix switches have been developed [2, 3]. Hybrid opto-electronics integration based on the terraced-silicon platform technologies are also important both to the fiber-to-the-home (FTTH) applications and high-speed signal processing devices [4, 5]. Synthesis theory of the lattice-form programmable optical filters has been developed [6] and implemented on the fabrication of variable group-delay dispersion equalizers [7]. This paper briefly reviews the recent progress in planar lightwave circuit devices for optical WDM systems and subscriber networks with particular emphasis on $N \times N$ arrayed-waveguide grating multiplexers and related devices such as optical add/drop multiplexers (ADM).

## 2. Waveguide fabrication

Planar lightwave circuits using silica-based optical waveguides are fabricated on silicon or silica substrate by a combination of flame hydrolysis deposition (FHD) and reactive ion etching (RIE). Fine glass particles are produced in the oxy-hydrogen flame and deposited on substrates. After depositing under-cladding and core glass layers, the wafer is heated to high temperature for consolidation. The circuit pattern is fabricated by photolithography

and reactive ion etching. Then core ridge structures are covered with over-cladding layer and consolidated again.

As the typical bending radius $R$ of silica waveguide is around 2–25 mm, the chip size of the large-scale integrated circuit becomes several centimetres square. Therefore, propagation loss reduction and the uniformity of refractive indices and core geometries throughout the wafer are strongly required. Propagation loss of 0.1 dB cm$^{-1}$ was obtained in a 2-m long waveguide with $\Delta = 2\%$ index difference ($R = 2$ mm) [8] and loss of 0.035 dB cm$^{-1}$ was obtained in a 1.6-m long waveguide with $\Delta = 0.75\%$ index difference ($R = 5$ mm) [9], respectively. Further loss reduction down to 0.017 dB cm$^{-1}$ has been achieved (Fig. 1) in a 10-m long waveguide with $\Delta = 0.45\%$ index difference ($R = 15$ mm) [10]. The higher loss for TM mode (electric field vector is perpendicular to the waveguide plane) may be due to the waveguide wall roughness caused by RIE etching process. However the mode conversion from TE to TM mode or *vice versa* was less than $-20$ dB in 10-m long waveguides. Various kinds of waveguides are utilized depending on the circuit configurations. The propagation losses of low-$\Delta$ and medium-$\Delta$ waveguides are about 0.01 dB cm and those of high-$\Delta$ and super high-$\Delta$ waveguides are about 0.04– 0.07 dB cm$^{-1}$, respectively. The low-$\Delta$ waveguides are superior to the high-$\Delta$ waveguides in terms of fibre coupling losses with the standard single-mode fibres. On the other hand, the minimum bending radii for high-$\Delta$ waveguides are much smaller than those of low-$\Delta$ waveguides. Therefore, high-$\Delta$ waveguides are indispensable in the construction of highly-integrated and large-scale optical circuits such as $N \times N$ star couplers, arrayed-waveguide grating multiplexers and dispersion equalizers.

## 3. Arrayed-waveguide grating
### 3.1. Principle of operation and fundamental characteristics
An $N \times N$ arrayed-waveguide grating multiplexer is very attractive in optical WDM networks since it is capable of increasing the aggregate transmission capacity of single strand optical fibre [11, 12]. The arrayed-waveguide grating consists of input/output waveguides, two focusing slab regions and a phase-array of multiple channel waveguides with the constant path length difference $\Delta L$ between neighboring waveguides (Fig. 2). In the first slab region, input waveguide separation is $D_1$, the array waveguide separation $d_1$, and the radius of curvature $f_1$, respectively. Generally the waveguide parameters in the first and the second slab regions may be different. Therefore, in the second slab region the
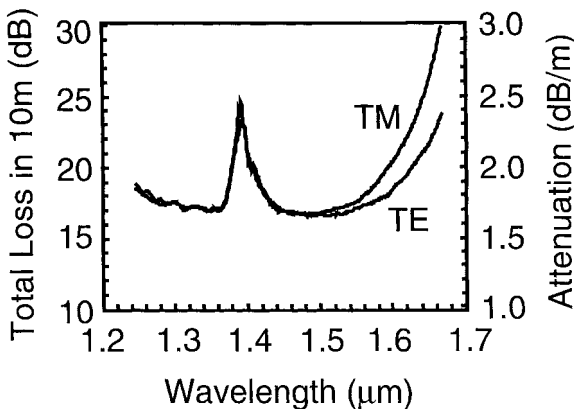


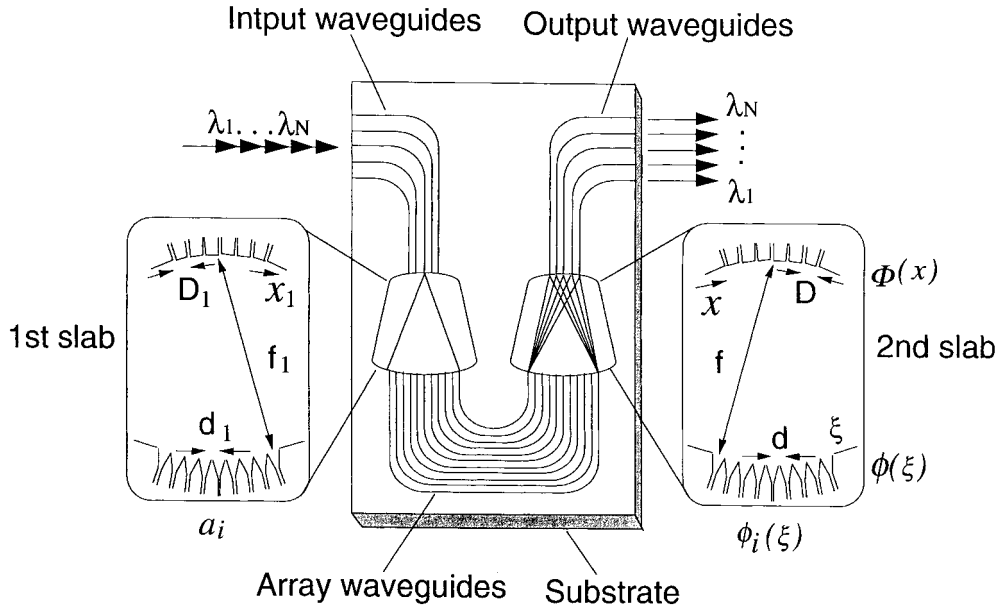*Figure 1* Loss spectra of 10-m long waveguide.

*Figure 2* Schematic configuration of arrayed-waveguide grating multiplexer.

output waveguide separation is $D$, the array waveguide separation is $d$, and the radius of curvature is $f$, respectively. The input light at the position of $x_1$ ($x_1$ is measured in clockwise direction from the center of input waveguides) is radiated to the first slab and then excites the arrayed waveguides. The excited electric field amplitude in each array waveguide is $a_i (i = 1 - N_{AWG})$ where $N_{AWG}$ is the total number of array waveguides. Amplitude profile $a_i$ is usually a Gaussian distribution. After traveling through the arrayed waveguides, the light beams constructively interfere into one focal point $x$ ($x$ is measured in clockwise direction from the center of output waveguides) in the second slab. The location of this focal point depends on the signal wavelength since the relative phase delay in each waveguide is given by $\Delta L / \lambda$. Figure 3 shows an enlarged view of the second slab region. Let us consider the phase retardations for the two light beams passing through the $(i - 1)$th and $i$th array waveguides. The geometrical distances of two beams in the second slab region are approximated as shown in Fig. 3. We have similar configurations in the first slab region as those in Fig. 3. The difference of the total phase retardations for the two light beams passing through the $(i - 1)$th and $i$th array waveguides must be an integer multiple of $2\pi$ in order that two beams constructively interfere at the focal point $x$. Therefore we have the interference condition as

$$\beta_s(\lambda_0)\left(f_1 - \frac{d_1 x_1}{2f_1}\right) + \beta_c(\lambda_0)[L_c + (i - 1)\Delta L] + \beta_s(\lambda_0)\left(f + \frac{dx}{2f}\right)$$
$$= \beta_s(\lambda_0)\left(f_1 + \frac{d_1 x_1}{2f_1}\right) + \beta_c(\lambda_0)[L_c + i\Delta L] + \beta_s(\lambda_0)\left(f - \frac{dx}{2f}\right) - 2m\pi \qquad (1)$$

where $\beta_s$ and $\beta_c$ denote the propagation constants in slab region and array waveguide, $m$ is an integer, $\lambda_0$ the center wavelength of WDM system and $L_c$ the minimum array waveguide length. Subtracting common terms from Equation 1, we obtain
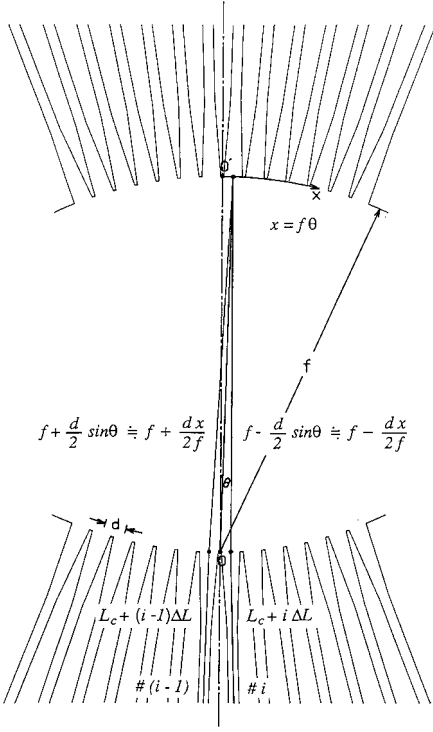
*Figure 3*  Enlarged view of the second slab region.

$$\beta_s(\lambda_0)\frac{d_1x_1}{f_1} - \beta_s(\lambda_0)\frac{dx}{f} + \beta_c(\lambda_0)\Delta L = 2m\pi \tag{2}$$

When the condition $\beta_c(\lambda_0)\Delta L = 2m\pi$ or

$$\lambda_0 = \frac{n_c\Delta L}{m} \tag{3}$$

is satisfied for $\lambda_0$, the light input position $x_1$ and the output position $x$ should satisfy the condition

$$\frac{d_1x_1}{f_1} = \frac{dx}{f} \tag{4}$$

In Equation 3 $n_c$ is an effective index of the array waveguide ($n_c = \beta_c/k$   $k$: wave number in vacuum) and $m$ is called as a diffraction order. The above equation means that when light is coupled into the input position $x_1$, the output position $x$ is determined by Equation 4. Usually the waveguide parameters in the first and the second slab regions are the same. Therefore input and output distances are equal as $x_1 = x$. The dispersion of the focal position $x$ with respect to the wavelength $\lambda$ for the fixed light input position $x_1$ is given by differentiating Equation 2 with respect to $\lambda$ as

$$\frac{\Delta x}{\Delta \lambda} = -\frac{N_c f \Delta L}{n_s d \lambda_0} \tag{5}$$

where $n_s$ is the effective index in the slab region, $N_c$ the group index of the effective index $n_c$ of the array waveguide ($N_c = n_c - \lambda \, dn_c/d\lambda$), respectively. The dispersion of the input-

side position $x_1$ with respect to the wavelength $\lambda$ for the fixed light output position $x$ is given by

$$\frac{\Delta x_1}{\Delta \lambda} = \frac{N_c f_1 \Delta L}{n_s d_1 \lambda_0} \tag{6}$$

The input and output waveguide separations are $|\Delta x_1| = D_1$ and $|\Delta x| = D$, respectively when $\Delta \lambda$ is the channel spacing of the WDM signal. Putting these relations into Equations 5 and 6, the wavelength spacing in output side for the fixed light input position $x_1$ is given by

$$\Delta \lambda_{\text{out}} = \frac{n_s d D \lambda_0}{N_c f \Delta L} \tag{7}$$

and the wavelength spacing in input side for the fixed light output position $x$ is given by

$$\Delta \lambda_{\text{in}} = \frac{n_s d_1 D_1 \lambda_0}{N_c f_1 \Delta L} \tag{8}$$

Generally the waveguide parameters in the first and the second slab regions are the same; they are, $D_1 = D$, $d_1 = d$ and $f_1 = f$. Then the channel spacings are the same as $\Delta \lambda_{\text{in}} = \Delta \lambda_{\text{out}} \equiv \Delta \lambda$. The path length difference $\Delta L$ is obtained from Equations 7 or 8 as

$$\Delta L = \frac{n_s d D \lambda_0}{N_c f \Delta \lambda} \tag{9}$$

The spatial separation of the $m$th and $(m + 1)$th focused beams for the same wavelength is given from Equation 2 as

$$X_{\text{FSR}} = x_m - x_{m+1} = \frac{\lambda_0 f}{n_s d} \tag{10}$$

$X_{\text{FSR}}$ represents the free spatial range of AWG. Number of available wavelength channels $N_{\text{ch}}$ is given by dividing $X_{\text{FSR}}$ with the output waveguide separation $D$ as

$$N_{\text{ch}} = \frac{X_{\text{FSR}}}{D} = \frac{\lambda_0 f}{n_s d D} \tag{11}$$

The electric field profile $\Phi(x)$ at the output plane of AWG (Fig. 2) is the summation of the farfield patterns of $\phi_i$'s from each array waveguide. Therefore, $\Phi(x)$ is the summation of the spatial Fourier transforms of $\phi_i$'s. Summation and Fourier transformation can be exchanged in the linear system. Then it is shown that the focused electric field profile $\Phi(x)$ at the output is the Fourier transform of the entire electric field profile $\phi(\xi)$ at slab–array interface.

Figure 4 shows the demultiplexing properties of 32ch-100 GHz spacing AWG. The AWG consists of 32 input/output waveguides, slab regions with arc length of 11.35 mm and waveguide array of 100 channel waveguides with the constant path length difference $\Delta L$ between neighboring waveguides. The path length difference $\Delta L$ is 63$\mu$m; the corresponding grating order at $\lambda_0 = 1.55\,\mu$m is $m = 59$ which gives a free spectral range of 25.6 nm (3.2 THz) and a channel spacing of 0.8 nm (100 GHz). Each arm in waveguide array consists of two straight waveguides of variable length on both sides and they are smoothly connected to a nonconcentric waveguide bend. The core size and refractive-index difference of the channel waveguides are 7 $\mu$m $\times$ 7 $\mu$m and 0.75% , respectively. The bending radius in the array varies from 5 to 6.3 mm and the minimum waveguide sepa-
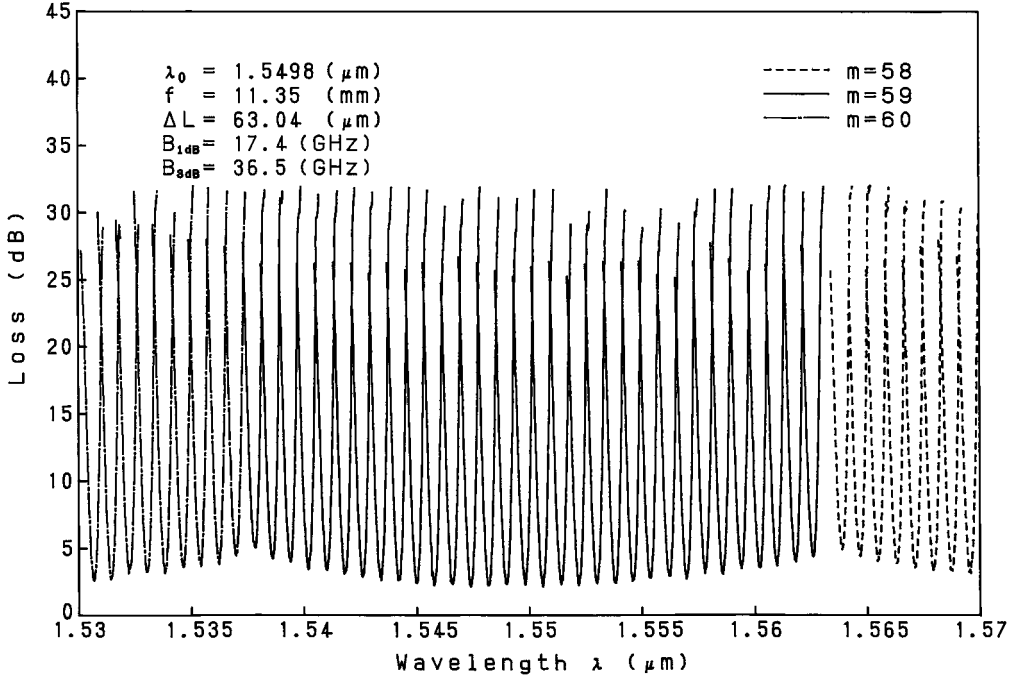
*Figure 4* Demultiplexing properties of 32ch-100 GHz spacing AWG.

ration is 30 μm. The total device size is 30 mm × 26 mm. The insertion losses for the peripheral output ports are 2–3 dB higher than those for the central output ports.

We have fabricated various kinds of multiplexers ranging 50-nm spacing 8-channel AWG to 25-GHz spacing 128-channel AWGs (Figs 5 and 6) [13, 14]. Table I summarizes experimental and theoretical performances of several kinds of AWG multiplexers. In all of these AWGs except 128ch AWG, crosstalks of about −30 dB have been obtained. Numbers in parentheses are the designed values ($\lambda_0$'s) and calculated values (3 dB band-widths) by BPM [15], respectively. Experimental results agree well with the theoretical values. The crosstalk in 128ch AWG is mainly determined by the sub-peaks near the main pass bands. If these sub-peaks are eliminated by the improvement of fabrication tech-niques and/or phase-error compensation techniques [16] which is described later, cross-talks can be improved by at least 10 dB down to −25 dB levels.

When some of the waveguide parameters in the first slab ($D_1, d_1$, and $f_1$) and those in the second slab region ($D$, $d$, and $f$) are different, the channel spacing $\Delta\lambda_{\text{out}}$ becomes different from $\Delta\lambda_{\text{in}}$ as shown in Equations 7 and 8. Putting $x_1 = jD_1$ and $x = jD(j = \pm 1, \pm 2, \pm 3, \ldots)$ in Equation 2, it can be rewritten as

$$n_{\text{s}}(\lambda)j\left(\frac{d_1 D_1}{f_1} - \frac{dD}{f}\right) + n_{\text{c}}(\lambda)\Delta L = m\lambda \tag{12}$$

The above equation is satisfied with the following center wavelength

$$\lambda = \lambda_0 + j\frac{N_c}{n_c}\left(\frac{d_1 D_1 f}{dDf_1} - 1\right)\Delta\lambda_{\text{out}} \tag{13}$$
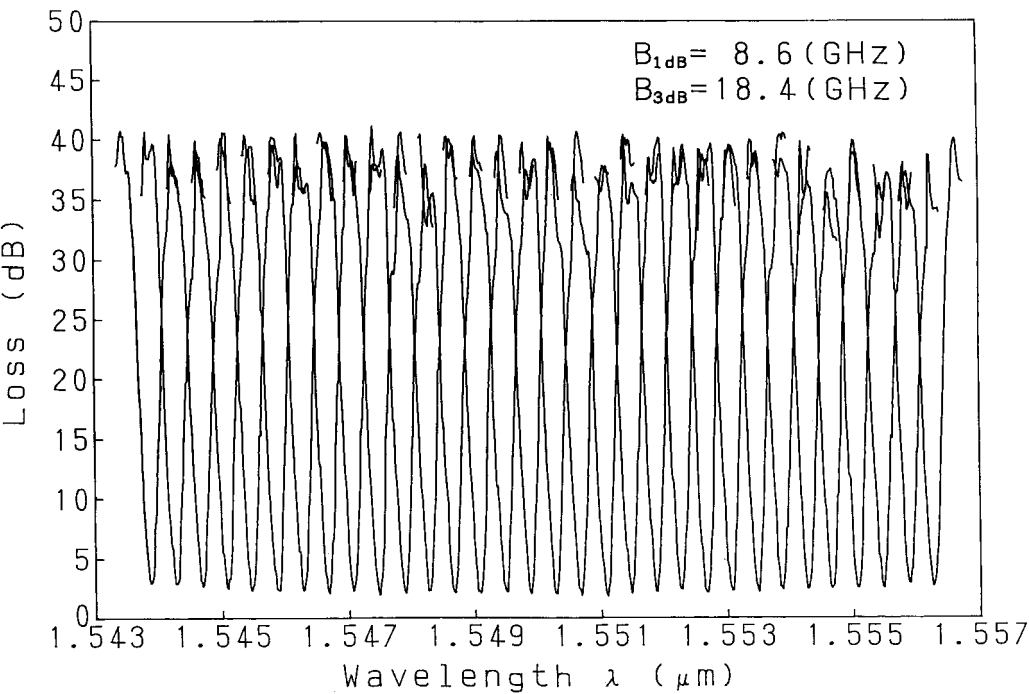
112

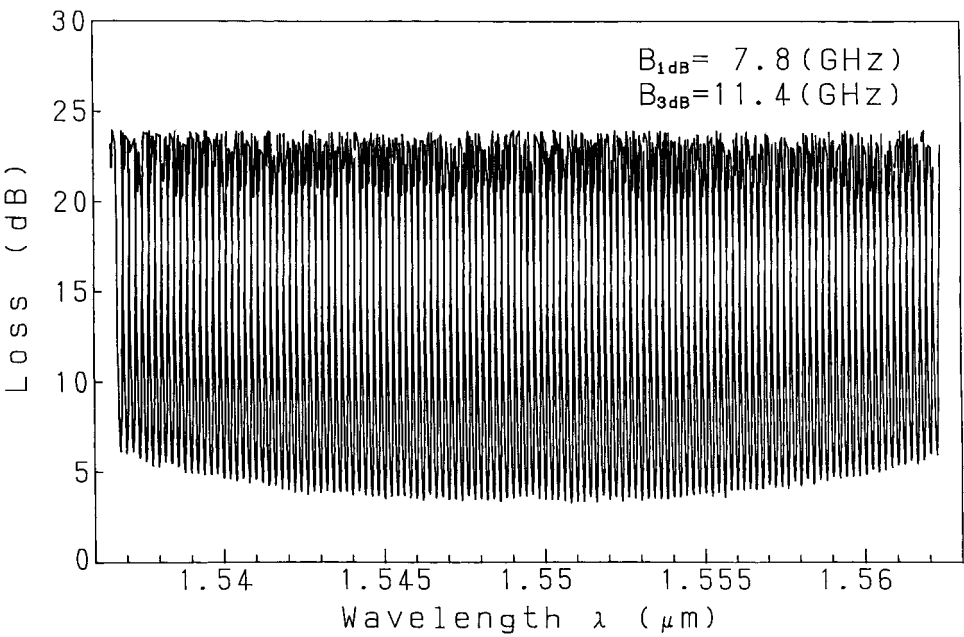*Figure 5* Demultiplexing properties of central 32 channels in 64ch-50 GHz spacing AWG.



*Figure 6* Demultiplexing properties of 128ch-25 GHz spacing AWG.

TABLE I  Experimental and theoretical performances of several kinds of AWG multiplexers

| Parameters | Experimental and Theoretical Results | | | | |
|---|---|---|---|---|---|
| Number of channels $N$ | 8 | 16 | 32 | 64 | 128 |
| Center wavelength $\lambda_0$ | 1.299 µm | 1.5521 µm | 1.5498 µm | 1.5496 µm | 1.5494 µm |
| (designed value) | (1.30 µm) | (1.552 µm) | (1.550 µm) | (1.550 µm) | (1.550 µm) |
| Channel spacing $\Delta\lambda$ | 50 nm | 2 nm | 0.8 nm = 100 GHz | 0.4 nm = 50 GHz | 0.2 nm = 25 GHz |
| Path difference $\Delta L$ | 2.8 µm | 50.3 µm | 63 µm | 63 µm | 63 µm |
| Slab arc length $f$ | 3.58 mm | 5.68 mm | 11.35 mm | 24.2 mm | 36.3 mm |
| Diffraction order $m$ | 3 | 47 | 59 | 59 | 59 |
| Number of arrayed-waveguides | 28 | 60 | 100 | 160 | 388 |
| On chip loss for $\lambda_0$ | 2.2 dB | 2.3 dB | 2.1 dB | 3.1 dB | 3.5 dB |
| 3-dB Bandwidth | 27.4 dB | 0.74 dB | 40 GHz | 19 GHz | 11 GHz |
| (BPM simulation) | (28.6 nm) | (0.75 nm) | (37 GHz) | (21 GHz) | (9.5 GHz) |
| Channel crosstalk | $< -26$ dB | $< -29$ dB | $< -28$ dB | $< -27$ dB | $< -16$ dB |

( ) $\cdots$ Designed values by beam propagation method.

where we used Equation 9. Equation 13 indicates that the center pass wavelength of AWG can be tuned up or down by choosing the proper $j$th input–output pair. Such vernier design was demonstrated [17] in which input and output waveguide separations $D_1$ and $D$ were different while $d_1 = d$, and $f_1 = f$. Vernier AWG can compensate for the possible center wavelength shift due to the slight fabrication error in waveguide parameters $n_c$ and $\Delta L$. Vernier AWG can also be realized by changing at least one of the waveguide parameters in the first slab ($D_1$, $d_1$, and $f_1$) and those in the second slab region ($D$, $d$ and $f$). Figure 7 shows the measured center wavelengths in array-side vernier 32ch-100 GHz AWG. The input and output waveguide separations in array-side vernier AWG was $d_1 = 18$ µm and $d = 20$ µm while $D_1 = D = 25$ µm, and $f_1 = f = 13.7$ mm. The straight line in Fig. 7 indicates the vernier line for the center path wavelengths. For the $1 \times N$ wavelength filter applications the vernier technique is quite effective to compensate for the possible fabrication errors in center wavelength of AWG.

## 3.2. Flat spectral response AWG
### 3.2.1. Parabola-type AWG

As the dispersion of the focal position $x$ with respect to the wavelength $\lambda$ is almost constant (Equation 5), the transmission loss of normal AWG monotonically increases around the center wavelength of each channel. This places tight restrictions on the wavelength tolerance of laser diodes and requires accurate temperature control for both AWGs and laser diodes. Moreover, since optical signals are transmitted through several filters in the WDM ring/bus networks, cumulative passband width of each channel becomes much narrower than that of the single-stage AWG filter. Therefore, flat and broadened spectral responses are required for AWG multiplexers. Several approaches have been proposed to flatten the passbands of AWGs [18–20]. We fabricated a novel flat-response AWG multiplexer having parabolic waveguide horns in the input waveguides [21]. Figure 8 shows the enlarged view of the interface between: (a) input waveguides and first slab and (b) second slab and output waveguides, respectively. The width of the parabolic horn along the propagation direction $z$ is given by [22]
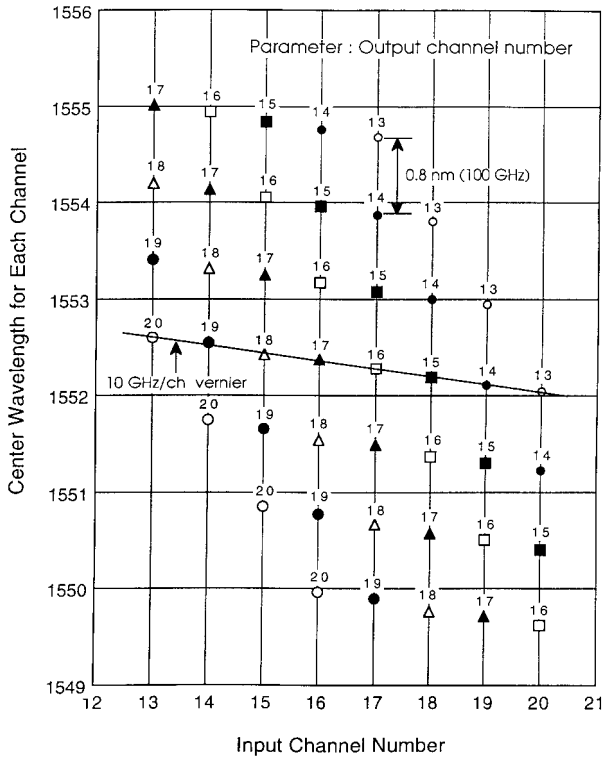
*Figure 7* Center wavelengths in array-side vernier AWG.

$$W(z) = \sqrt{2\alpha\lambda_{\mathrm{g}}z + (2a)^2} \tag{14}$$

where $\alpha$ is a constant less than unity, $\lambda_{\mathrm{g}}$ the wavelength in the guide ($\lambda_{\mathrm{g}} = \lambda/n_{\mathrm{eff}}$) and $2a$ the core width of the channel waveguide , respectively. At the proper horn length $z = \ell$ less than the collimator length, a slightly double-peaked intensity distribution can be obtained. A broadened and sharp falling optical intensity profile is obtainable by the parabolic waveguide horn, which is quite advantageous for achieving wide passband without dete-



(a)

(b)
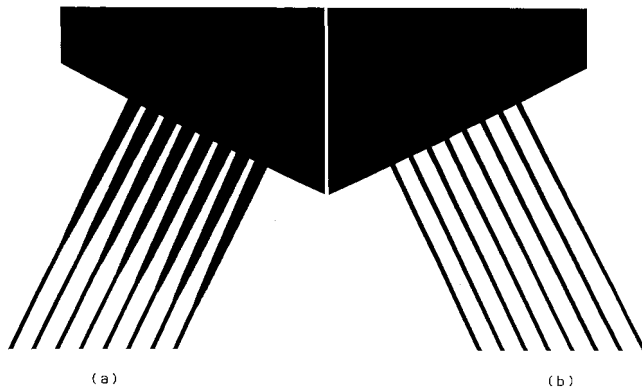
*Figure 8* Enlarged view of the interface between (a) input waveguides and first slab and (b) second slab and in flat response 8ch AWG.

115

riorating the nearest neighbor crosstalk characteristics. The broadened and double-peaked field is imaged onto the entrance of an output waveguide having normal core width. The overlap integral of the refocused field with the local normal mode of the output waveguide gives the flattened spectral response of AWG. Figure 9 shows the demultiplexing properties of 16ch-100 GHz spacing AWG having parabolic horns with $W = 40\,\mu$m and $z = 800\,\mu$m. The crosstalks to the neighboring channels are less than $-35$ dB and the on-chip loss is about 7.0 dB. The average 1-, 3- and 20-dB bandwidths are 86.4, 100.6 and 143.3 GHz, respectively.

### 3.2.2. Sinc-type AWG

It has been confirmed that in order to obtain a flat spectral response, it is necessary to produce the rectangular electric field profile at the focal plane (interface between the second slab and output waveguides). As the electric field profile in the focal plane is the Fourier transform of the field in the array output aperture (interface between the array waveguide and second slab), such a rectangular field profile could be generated when the electric field at the array output aperture obeys a $\sin(\xi)/\xi$ distribution where $\xi$ is measured along the array output aperture [18]. Figure 10 shows the electric field amplitude and relative phase delays (excess phase value added to $i \times \Delta L$ where $i$ denotes the $i$th array waveguide) in the sinc-type flat response AWG measured by the low coherence Fourier transform spectroscopy [23]. Sinc-shaped electric field amplitude distribution was realized by introducing an additional loss to each array waveguide. The excess path length differences of $\pi$ for the negative sinc values were realized by the additional path length $\delta\ell = \lambda/2n_c$ to the corresponding array waveguides. The crosstalk and flat passband
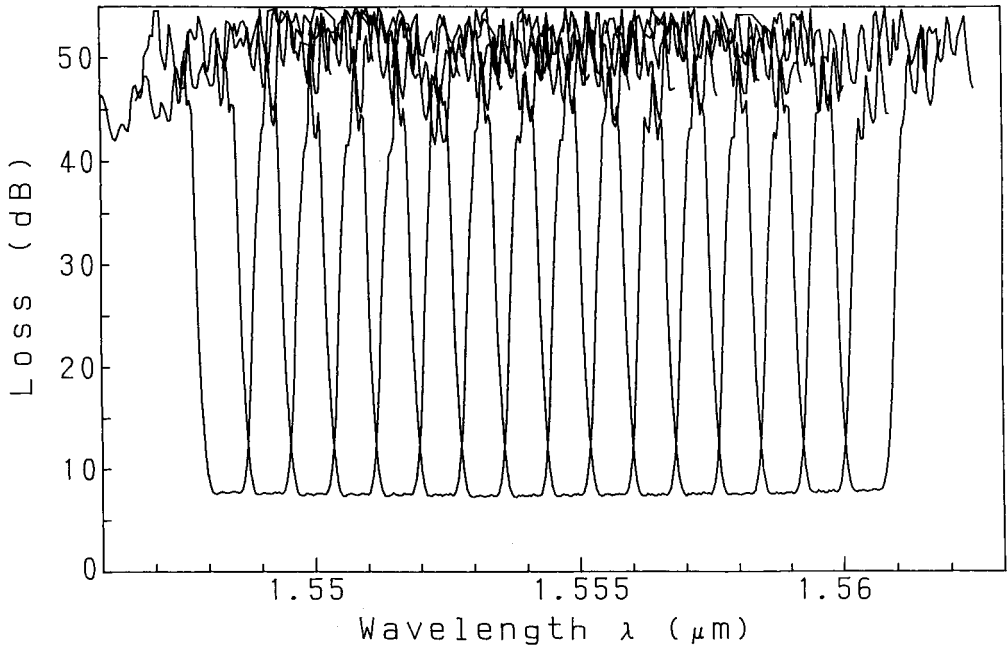


*Figure 9* Demultiplexing properties of 16ch-100 GHz spacing AWG having parabolic horns with $W = 40\,\mu$m and $z = 800\,\mu$m.
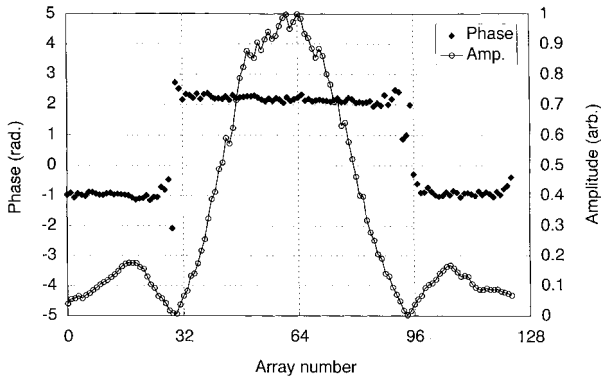
Figure 10 Electric field amplitude and relative phase delays in the sinc-type flat response AWG.

characteristics are almost the same as those of parabola-type AWGs; they are, the cross-talks to the neighboring channels are less than -30 dB and the on-chip loss is about 7.0 dB. The average 1-, 3- and 20-dB bandwidths are 63 GHz, 82 and 140 GHz, respectively.

## 3.3. Athermal (temperature insensitive) AWG

Temperature sensitivity of the pass wavelength (frequency) in the silica-based AWG is about $d\lambda/dT = 1.2 \times 10^{-2} (\text{nm deg}^{-1})$ $(d\nu/dT = -1.5(\text{GHz deg}^{-1}))$, which is mainly determined by the temperature dependence of silica glass itself $(dn_c/dT = 1.1 \times 10^{-5}(\text{deg}^{-1}))$. The AWG multiplexer should be temperature controlled with a heater or a Peltier cooler to stabilize the channel wavelengths. This requires the constant power consumption of few watts and a lot of equipments for the temperature control. We have fabricated an athermal (temperature insensitive) AWG operating in the 0–85°C temperature range [24]. Figure 11 shows a schematic configuration of athermal AWG. Temperature-dependent optical path difference in silica waveguides is compensated with a triangular groove filled with silicone adhesive which has negative thermal coefficient. As the pass wavelength is given by $\lambda_0 = n_c \Delta L/m$, optical path length difference $n_c \Delta L$ should be made insensitive to temperature. Therefore the groove is designed to satisfy the following conditions

$$n_c \Delta L = n_c \Delta \ell + \hat{n}_c \Delta \hat{\ell} \tag{15}$$

$$\frac{d(n_c \Delta L)}{dT} = \frac{dn_c}{dT} \Delta \ell + \frac{d\hat{n}_c}{dT} \Delta \hat{\ell} = 0 \tag{16}$$

where $\hat{n}_c$ is the refractive index of silicone and $\Delta \ell$ and $\Delta \hat{\ell}$ are the path length differences of silica waveguides and silicone region. Equation 15 is a condition to satisfy the AWG
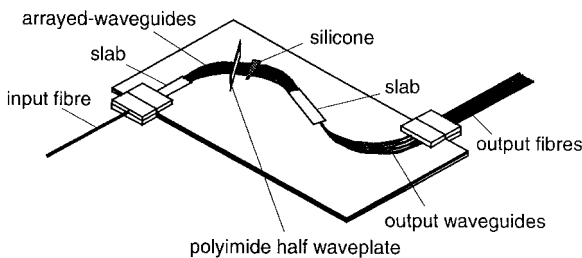


Figure 11 Schematic configuration of athermal AWG.

117

specifications and Equation 16 is the athermal condition, respectively. The temperature sensitivity of silicone is $d\hat{n}_c/dT = -37 \times 10^{-5}(\deg^{-1})$. Therefore the path length difference of silicone is $\Delta\hat{\ell} \cong \Delta\ell/37$. Figure 12 shows temperature dependencies of pass wavelengths in conventional and athermal AWGs. The temperature-dependent wavelength change has been reduced from 0.95 to 0.05 nm in the 0–85°C range. The excess loss caused by the groove is about 2 dB which is mainly a diffraction loss in the groove. During the heat cycle test from −40 to 85°C , the loss change is smaller than 0.2 dB. Furthermore, the channel wavelength change was less than 0.02 nm in a long-term test over 5000 h at 75°C and 90% relative humidity.

## 3.4. Phase error compensation of AWG

Crosstalk improvement is the major concern for the AWG multiplexers, especially for $N \times N$ routing applications [25]. Crosstalks to other channels are caused by the sidelobes of the focused beam in the second slab region. These sidelobes are mainly attributed to the phase fluctuations of the total electric field profile at the output side array–slab interface since the focused beam profile is the Fourier transform of the electric field in the array waveguides (Fig. 2). The phase errors are caused by the nonuniformity of effective-index and/or core geometry in the arrayed-waveguide region. We measured the phase errors in the AWGs by using Fourier transform spectroscopy [23]. Figure 13 shows the measured phase error distribution in 16ch-100 GHz spacing AWG. Measured crosstalk of the multiplexer is about −30 dB as shown by open circles in Fig. 14. As phase errors with low spatial frequency generates sidelobes near the main focused beam, the slow phase variations are most harmful for the crosstalk characteristics. The peak-to-peak phase fluctuation in Fig. 13 is about ±10° over the 20 mm average path length $L$ ($\approx 13\,000\lambda$). 10° phase variation over 20 mm path length corresponds to $2.1 \times 10^{-6}$ effective-index fluctuation in the array waveguides. If the phase errors were eliminated, we could obtain about −40 dB crosstalk in 100 GHz spacing AWG as shown by the theoretical curve in Fig. 14. The reason why we could not obtain infinitely lower crosstalk is that there still remains the amplitude errors. This calculation curve takes into account the measured amplitude distributions in the 16ch-100 GHz spacing AWG. Therefore we should note here that even
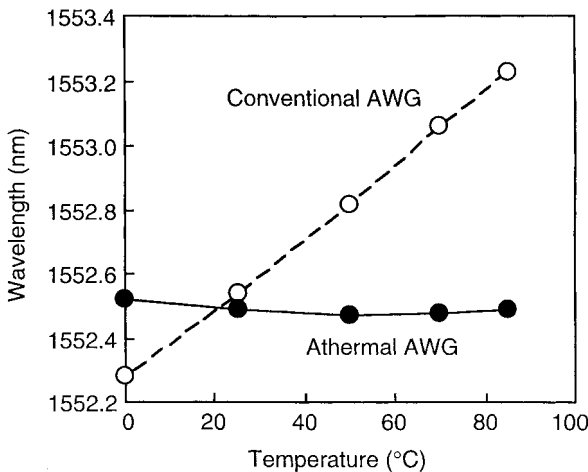


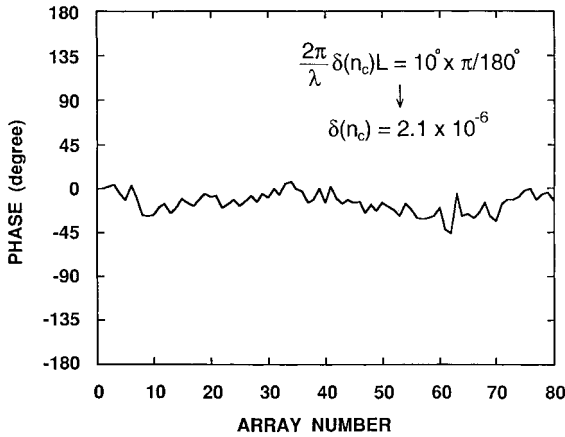Figure 12 Temperature dependences of pass wavelengths.

*Figure 13* Measured phase error distribution in 16ch 100 GHz spacing AWG.

when phase errors were eliminated, crosstalks are generated by the amplitude errors (amplitude irregularities) of the electric field profile.

In order to improve the crosstalk characteristics of AWGs, we carried out the phase error compensation experiment using 16 ch-10 GHz spacing ultra-narrow AWG filter [26]. Figure 15 shows the configuration of phase-compensated AWG using an a-Si film for phase trimming. The path length difference of AWG is $\Delta L = 1271\,\mu m$ in 64 array waveguides. As array waveguide region occupies large area, accumulated phase errors become quite large. Therefore the crosstalk of AWG without phase error compensation was about $-8\,dB$. An a-Si stress-applying film was deposited on top of the overcladding of each array waveguide and the amount of stress-optic effect was adjusted by the Ar ion laser trimming (evaporation) of a-Si film length. Figure 16 shows phase error distributions before and after phase compensation. The peak-to-peak fluctuation is reduced to about $\pm 2°$ over the 60 mm average path length. The effective-index fluctuations are reduced to within $1.2 \times 10^{-7}$. Figure 17 shows the measured demultiplexing properties of phase compensated
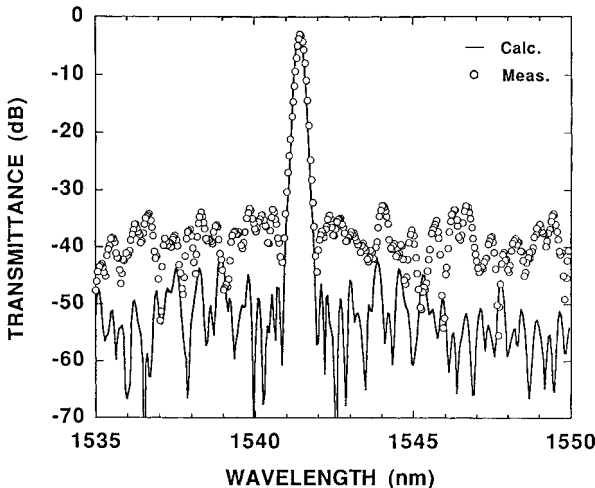


*Figure 14* Theoretical transmittance without phase errors (solid line) and measured result with phase errors (circle).
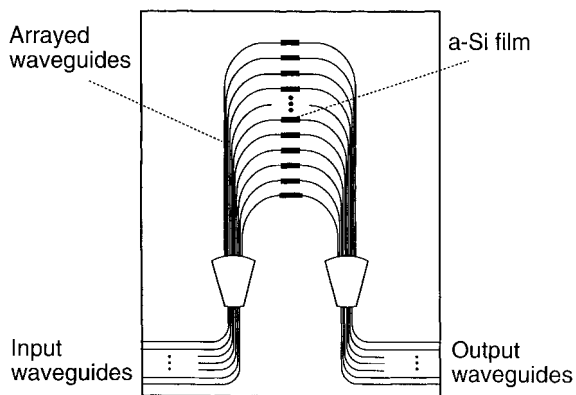
119

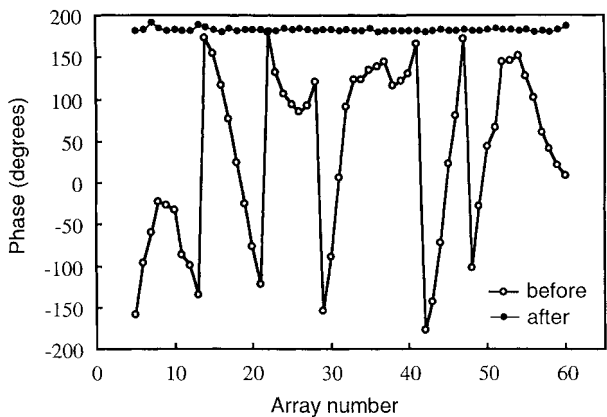*Figure 15* Configuration of phase-compensated AWG with a-Si film.



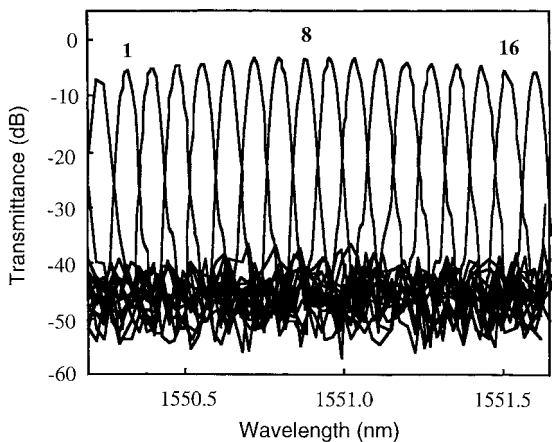*Figure 16* Phase error distributions for the TE mode before and after phase compensation.



*Figure 17* Transmittance of phase-compensated 16ch 10 GHz spacing AWG.

16ch-10 GHz spacing AWG. Crosstalks to the neighboring and all other channels are less than −31 dB.

## 4. Optical add/drop multiplexer

An optical add/drop multiplexer (ADM) is a device that gives simultaneous access to all wavelength channels in a WDM communication systems. We proposed a novel optical ADM and demonstrated the basic functions of individually routing 16 different wavelength channels with 100-GHz channel spacing [27]. The waveguide configuration of 16ch optical ADM is shown in Fig. 18. It consists of four arrayed-waveguide gratings and 16 double-gate thermo-optic (TO) switches. Four AWGs are allocated with crossing their slab regions each other. These AWGs have the same grating parameters; they are, the channel spacing of 100 GHz and the free spectral range of 3300 GHz (26.4 nm) at 1.55 μm region. Equally spaced WDM signals, $\lambda_1, \lambda_2, \ldots, \lambda_{16}$ which are coupled to the main input port (add port) in Fig. 18 are first demultiplexed by the $AWG_1(AWG_2)$ and then 16 signals are introduced into the left-hand side arms (right-hand side arms) of double-gate TO switches. The crossangle of the intersecting waveguides is designed to be larger than $30°$ so as to make the crosstalk and insertion loss negligible. Any optical signal coupled into the double-gate TO switch passes through the crossport of one of the four Mach–Zehnder interferometers (MZIs) before reaching the output port. In the single-stage MZI, the light extinction characteristics of the crossport is much better than that of the through
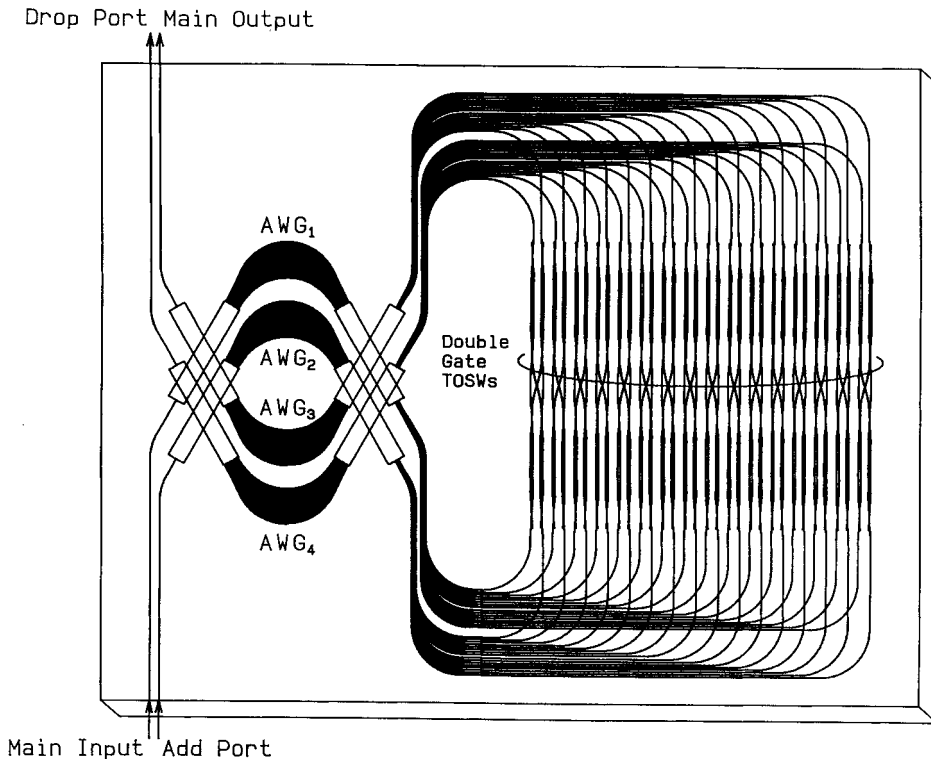


*Figure 18* Waveguide configuration of 16ch optical ADM with double-gate TO switches.

port even when the coupling ratio of directional coupler is deviated from 3 dB [28]. Therefore, the crosstalk of double-gate switch becomes substantially improved than that of the conventional single-stage TO switch. We designate here the "off" state of double-gate switch as the switching condition where signal from left input port (right input port) goes to right output port (left output port). The "on" state is then designated as the condition where signal from left input port (right input port) goes to left output port (right output port). When double-gate switch is "off", the demultiplexed light by $AWG_1(AWG_2)$ goes to the crossarm and multiplexed again by the $AWG_3(AWG_4)$. On the other hand, if double-gate switch is "on" state the demultiplexed light by $AWG_1(AWG_2)$ goes to the through arm and multiplexed by the $AWG_4(AWG_3)$. Therefore, any specific wavelength signal can be extracted from the main output port and led to the drop port by changing the corresponding switch condition. A signal at the same wavelength as that of the dropped component can be added to the main output port when it is coupled into add port in Fig. 18. When TO switches $SW_2$, $SW_4$, $SW_6$, $SW_7$, $SW_9$, $SW_{12}$, $SW_{13}$ and $SW_{15}$, for example, are turned to "on" the selected signals $\lambda_2$, $\lambda_4$, $\lambda_6$, $\lambda_7$, $\lambda_9$, $\lambda_{12}$, $\lambda_{13}$ and $\lambda_{15}$ are extracted from main output port (solid line) and led to the drop port (dotted line) as shown in Fig. 19. The on–off crosstalk is smaller than −30 dB with the on-chip losses of 8– 10 dB. As optical signals pass through both $AWG_3$ and $AWG_4$ the crosstalk level here is determined by the crosstalk in the arrayed-waveguides. Although the electric power necessary to drive double-gate switch becomes two times larger than the conventional TO switch, the power consumption itself can be reduced to almost 1/5–1/2 when we use the bridge-suspended phase shifters [29]. The present optical ADM can transport all input
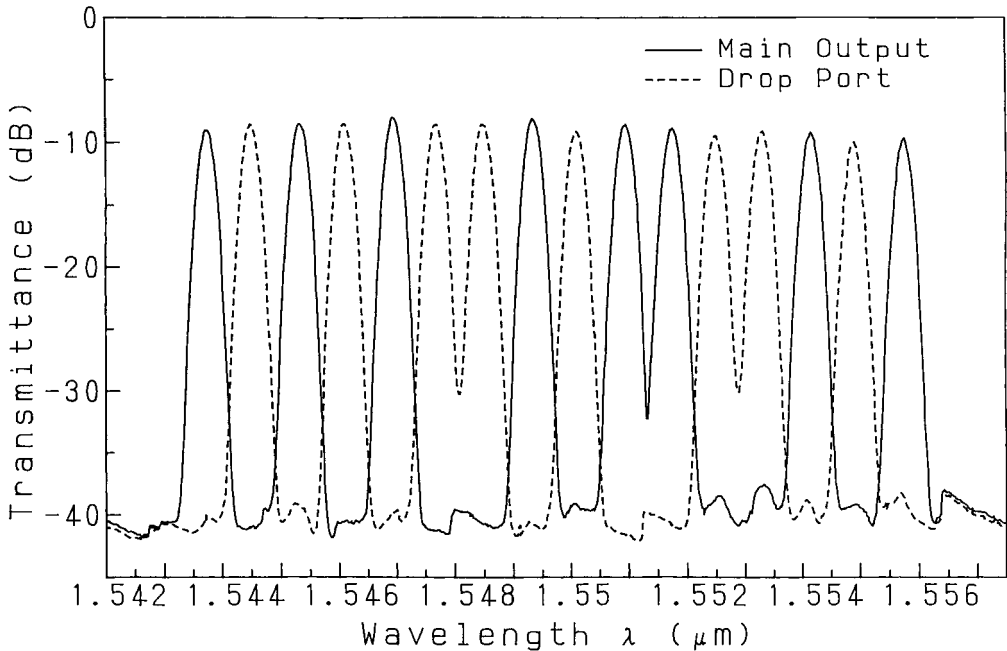


*Figure 19* Transmission spectra from main input port to main output port and drop port when TO switches $SW_2, SW_4, SW_6, SW_7, SW_9, SW_{12}, SW_{13}$ and $SW_{15}$ are "on".

signals to the succeeding stages without inherent power losses. Therefore, these ADMs are very attractive for all optical WDM routing systems and allow the network to be transparent to signal formats and bit rates.

## 5. Lattice-form programmable dispersion equalizers

The transmission distance in optical fibre communications has been greatly increased by the development of erbium-doped fibre amplifiers. In consequence, the main factor limiting the maximum repeater span is now the fibre chromatic dispersion. Several techniques have been reported to compensate for the delay distortion in optical stage [30–35]. An advantage of the PLC optical delay equalizer [34, 35] is that variable group-delay characteristics can be achieved by the phase control of silica waveguides. The basic configuration of the PLC delay equalizer is shown in Fig. 20. It consists of $N(=8)$ asymmetrical Mach–Zehnder interferometers and $N + 1 (= 9)$ tunable couplers, which are cascaded alternately in series. The crossport transfer function of the optical circuit is expressed by a Fourier series as

$$H(z) = \sum_{k=0}^{N} a_k z^{-k+N/2}, \qquad (17)$$

where $z$ denotes $\exp(j2\pi v \Delta t)$ ($v$ : optical frequency, $\Delta t = n_c \Delta L/c$: unit delay time difference in asymmetrical MZ interferometer) and $a_k$ is the complex expansion coefficient. The circuit design procedures are as follows. First the equalizer transfer function to be realized is expressed by the analytical function. Then coefficient $a_k{'}$ are determined by expanding the analytical function into a Fourier series. Finally coupling ratio ($\phi_i$) and phase shift value ($\theta_i$) in each stage of lattice filter are determined by the filter synthesis method [6].

In ultra-high speed optical fibre transmission systems ($>100\,\text{Gbit}s^{-1}$), the effect of the higher-order dispersion (third-order dispersion or dispersion slope) in the dispersion
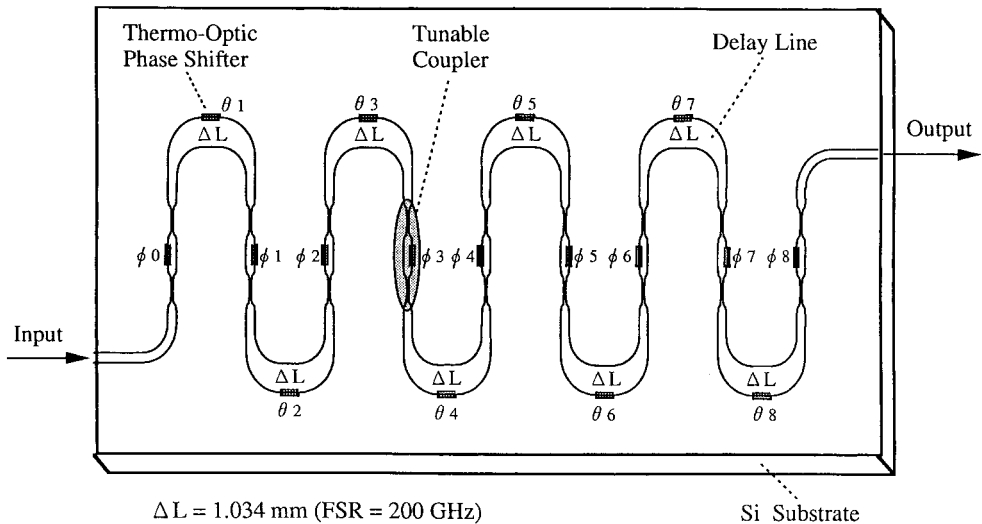


*Figure 20* Basic configuration of the PLC equalizer.

shifted fibre (DSF) is one of the major factors limiting the transmission distance [36]. Programmable dispersion equalizers can be designed so as to compensate for the higher-order dispersion of DSFs. Figure 21a shows the measured power transmittance and relative delay time of the PLC higher-order dispersion equalizer [37]. The dispersion slope of the equalizer is calculated to be $-15.8$ ps nm$^{-2}$. Figure 21b is the relative delay of the 300-km DSF. The dispersion slope of DSF is 0.05–0.006 ps nm$^{-2}$ km$^{-1}$. Therefore, the equalizer can compensate the higher-order dispersion of $\sim$300-km of DSF. Figure 21c shows the relative delay time of 300-km DSF cascaded with the equalizer. The positive dispersion slope of the DSF is almost completely compensated by the PLC equalizer.
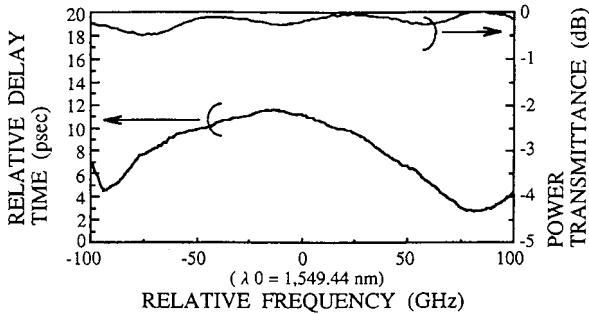


## (a) Higher-Order Dispersion Equalizer
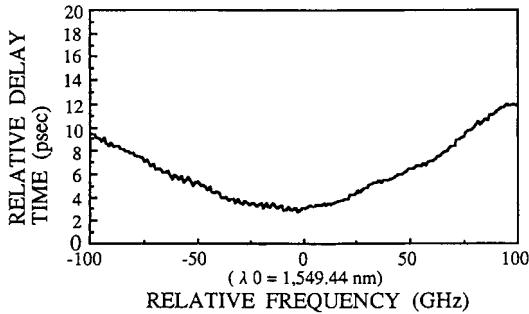


## (b) 300-km Dispersion Shifted Fiber
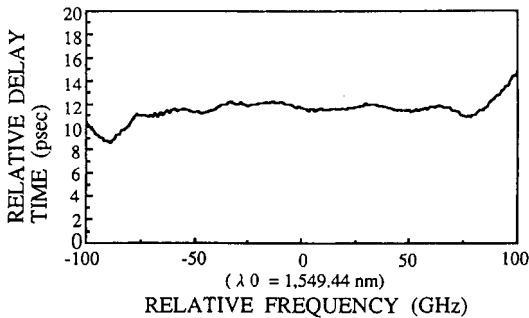


## (c) 300-km DSF + Equalizer

*Figure 21* Relative delay times of: (a) PLC higher order dispersion equalizer, (b) 300-km DSF and (c) 300-km DSF + equalizer.

200 Gbit s$^{-1}$ time-division-multiplexed transmission experiment using a dispersion slope equalizer has been carried out over 100-km fibre length [38]. The pulse distortion caused by the dispersion slope was almost completely recovered, and the power penalty was improved by more than 4 dB.

## 6. Hybrid integration technology using PLC platforms

It is widely recognized that optical hybrid integration is potentially a key technology for fabricating advanced integrated optical devices [4]. A silica-based waveguide on a Si substrate is a promising candidate for the hybrid integration platform since high-performance PLCs have already been fabricated using silica-based waveguides and Si has highly stable mechanical and thermal properties which make it a suitable optical bench. Figure 22 shows the PLC platform fabrication process [39]. First, a thick undercladding is deposited on a Si substrate with a terraced region using FHD, and then the surface of the substrate is flattened by mechanical polishing. To minimize the optical coupling loss between the opto-electronics (OE) device on the terrace and optical waveguide, a thin layer is deposited on the polished substrate surface. The thickness of the layer corresponds to the height of the active region of OE device on the terrace. Then, a core layer is deposited and patterned into a core ridge by RIE. The core ridge is then covered by the overcladding layer. Finally, RIE is used to form the Si terrace for the OE devices on the PLC and the terrace surface is exposed. The relative positions of the core and Si terrace surface are determined precisely because the terrace acts as an etch-stop layer during the RIE process. As a result, Si terrace functions as both a high-precision alignment plane and heatsink when OE device is flip-chip bonded on the terrace.

PLC platform technology has also been utilized in the fabrication of a hybrid integrated external cavity laser [40]. Figure 23 shows the configuration of multi-wavelength external cavity laser which consists of spot-size converted lasers (SS-LDs) [41] and a UV written
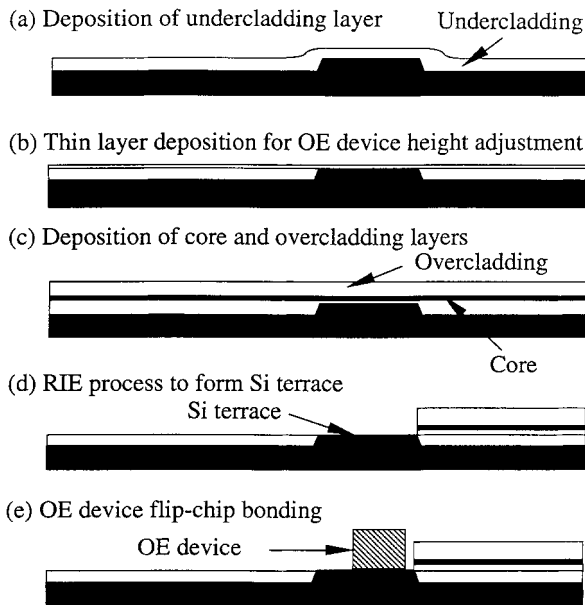
(a) Deposition of undercladding layer — Undercladding

(b) Thin layer deposition for OE device height adjustment

(c) Deposition of core and overcladding layers — Overcladding — Core

(d) RIE process to form Si terrace — Si terrace

(e) OE device flip-chip bonding — OE device

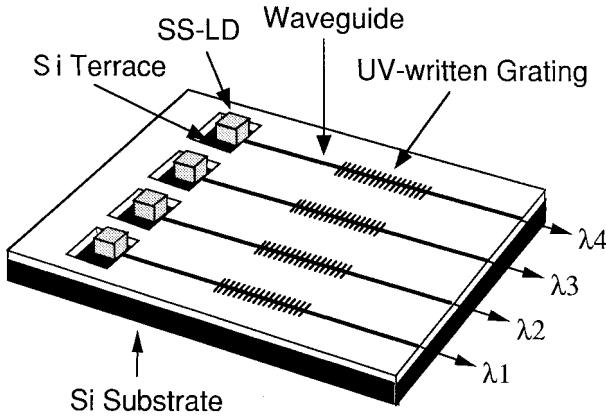Figure 22 PLC platform fabrication process.

*Figure 23* Configuration of hybrid integrated multi-wavelength external cavity laser.

grating [42]. Bragg gratings with 2-nm wavelength interval are written into each waveguide by ArF excimer laser irradiation through phasemasks. Figure 24 shows the measured output spectra. Each laser operates in a single longitudinal mode with a side-mode suppression of 40 dB. The temperature sensitivity of the oscillation frequency is $-1.7\,\mathrm{GHz\,deg^{-1}}$, which is one-eighth of the DFB lasers. Four channel simultaneous modulation experiment has been successfully carried out at 2.5 Gbit s$^{-1}$ [43]. Temperature stable multi-wavelength source will play an important role in WDM transmission and access network systems.

Semiconductor optical amplifier (SOA) gate switches having spot-size converters on both facets have been successfully hybrid-integrated on PLC platforms to construct high-speed wavelength channel selectors and $4 \times 4$ optical matrix switches [44, 45]. Figure 25 shows the configuration of 8-ch optical wavelength selector module. It consists of two AWG chips with 75-GHz channel spacing and hybrid integrated SOA gate array chip. It selects and picks up any wavelength channel from a multiplexed signals by activating the corresponding SOA gate switch. Three PLC chips are directly attached with each other
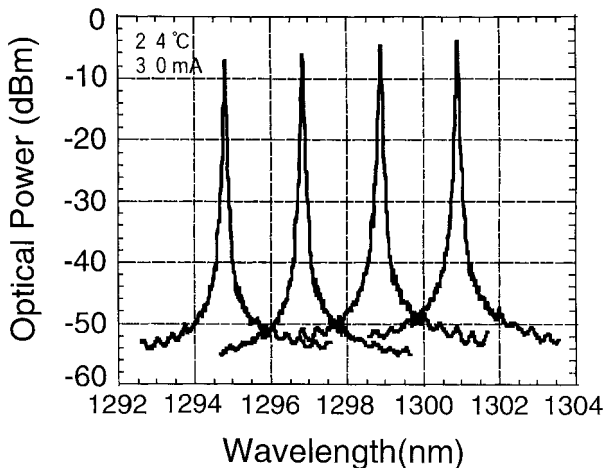


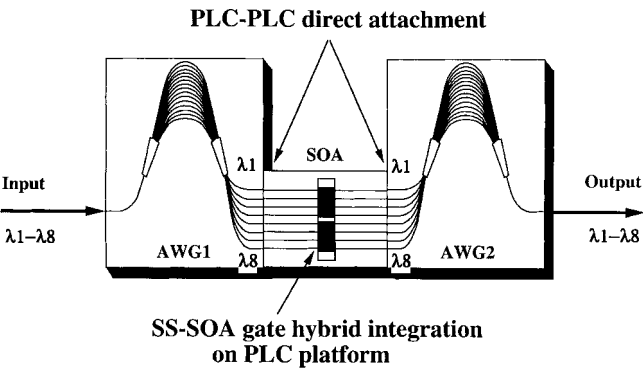*Figure 24* Oscillation spectra of 4-wavelength laser.

Figure 25 Configuration of 8-ch optical wavelength selector module.

using UV curable adhesive. The length of SOA gate switch is 1200 µm and their separation is 400 µm. The coupling loss between SOA and PLC waveguide ranges from 3.9 to 4.9 dB. Figure 26 shows the optical transmission spectra of the wavelength channel selector when only one SOA gate switch is activated successively. SOA injection current is 50 mA for all SOAs. The peak transmittances have 1–3 dB gains; they are, 16–19 dB total chip losses and fibre coupling losses are compensated by SOA gains. The crosstalk is less than −50 dB and the polarization-dependent loss is smaller than 1.4 dB, respectively. However, the crosstalk becomes about −30 dB when two or more SOA gate switches are activated simultaneously. The crosstalk in multi-gate operation is determined by the crosstalk of AWGs. In the high-speed switching experiments, the rise and fall time is confirmed to be less than 1 ns.

## 7. Summary

Recent progress in planar lightwave circuits have been reviewed. Although silica-based waveguides are simple circuit elements, various functional devices are fabricated by
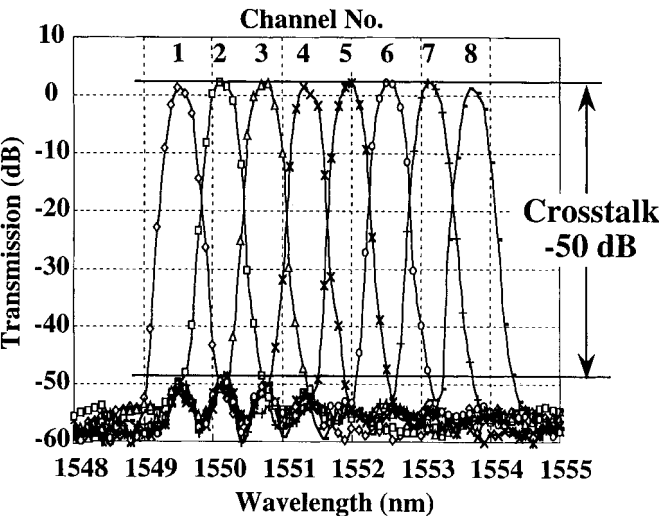


Figure 26 Optical transmission spectra of the wavelength channel selector when only one SOA gate switch is activated successively.

utilizing spatial multi-beam or temporal multi-stage interference effects such as arrayed-waveguide grating multiplexers and lattice-form programmable filters. Hybrid integration technologies will further enable us to realize much more functional and high-speed devices. The PLC technologies supported by continuous improvements in waveguide fabrication, circuit design and device packaging will further proceed to a higher level of integration of optics and electronics aiming at the next generation of telecommunication systems.

## Acknowledgements

## References

1. M. KAWACHI, *Opt. Quantum Electron.* **22** (1990) 391–416.
2. K. OKAMOTO, in Photonic Networks (Springer, Berlin,1997) pp. 118–132.
3. A. HIMENO *et al.*, in Photonic Networks (Springer-Verlag, Berlin, 1997) pp. 172–182.
4. Y. YAMADA *et al.*, *Electron. Lett.* **31** (1995) 1366–1367.
5. Y. AKAHORI *et al.*, Proc. IOOC/ECOC '97, **2** (1997) 359–362.
6. K. JINGUJI *et al.*, IEEE J. *Lightwave Tech.* **13** (1995) 73–82.
7. K. TAKIGUCHI *et al. Electron. Lett.* **31** (1995) 1240–1241.
8. S. SUZUKI *et al. Electron. Lett.* **28** (1992) 1863–1864.
9. Y. HIBINO *et al. Electron. Lett.* **29** (1993) 1847–1848.
10. Y. HIDA *et al. IPR'95*, (Dana Point, CA, 1995).
11. M. K. SMIT, *Electron. Lett.* **24** (1988) 385-386.
12. H. TAKAHASHI *et al. Electron. Lett.* **26** (1990) 87–88.
13. K. OKAMOTO *et al. Electron. Lett.* **31** (1995) 184–185.
14 K. OKAMOTO *et al. Electron. Lett.*, **32** (1996) 1474–1476.
15. W. P. HUANG *et al. J. Lightwave Tech.* **10** (1992) 295–305.
16. H. YAMADA *et al. Electron. Lett.* **33** (1997) 1698–1699
17. H. UETSUKA *et al.* Proc. OFC '95 Tu07, 1995, p.276.
18. K. OKAMOTO *et al. Opt. Lett.* **20** (1995) 43–45.
19. M. R. AMERSFOORT *et al. Electron. Lett.* **32** (1996) 449–451.
20. D. TROUCHET *et al.* Proc. OFC '97 ThM7, (Dallas, Texas, 1997).
21. K. OKAMOTO *et al. Electron. Lett.* **32** (1996) 1661–1662.
22. W. K. BURNS *et al. Appl. Phys. Lett.* **30** (1996) 28–30.
23. K. TAKADA *et al. Electron. Lett.* **30** (1994) 1671–1672.
24. Y. INOUE *et al. Electron. Lett.* **33** (1997) 1945–1946.
25. C. DRAGONE *et al. Photon. Tech. Lett.* **3** (1991) 896–899.
26. H. YAMADA *et al. Electron. Lett.* **32** (1996) 1580–1582.
27. K. OKAMOTO *et al. Electron. Lett.* **32** (1996) 1471–1472.
28. K. OKAMOTO *et al. Electron. Lett.* **31** (1995) 723–724.
29. A. SUGITA *et al.* Proc. of IOOC '89, 1989, Paper 18D1-4, p. 58
30. K. OKAMOTO *et al. IEEE J. Lightwave Tech.*, **11** (1993) 1325–1330.
31. M. ASHISH *et al.* OFC '93 Postdeadline paper PD13, (San Jose, 1993).
32. A. H. GNAUCK *et al. IEEE Photonics Tech. Lett.* **5** (1993) 663–666.
33. K. O. HILL *et al. Electron. Lett.* **30** (1994) 1755–1756.
34. K. TAKIGUCHI *et al. IEEE Photonics Tech. Lett.* **6** (1994) 86–88.
35. K. TAKIGHUCHI *et al. Electron. Lett.* **31** (1995) 2192–2193.
36. S. KAWANISHI *et al. Electron. Lett.* **31** (1995) 816–817.
37. K. TAKIGUCHI *et al. Electron. Lett.* **32** (1996) 755–757.
38. K. TAKIGUCHI *et al. Electron. Lett.* **32** (1996) 2083–2084.
39. Y. YAMADA *et al. Electron. Lett.* **29** (1993) 444–445.
40. T. TANAKA *et al. Electron. Lett.* **32** (1996) 1202–1203.

41. Y. TAHMORI *et al. Electron. Lett.* **31** (1995) 1069–1070.
42. T. TANAKA *et al.* OECC'97 10D3-3 (Seoul, Korea, 1997).
43. H. TAKAHASHI *et al.* IOOC-ECOC '97, (Edinburgh, UK, 1997) pp. 355–358.
44. I. OGAWA *et al.* Proc. OFC'98 postdeadline paper PDP4 (San Jose, CA, 1998).
45. T. KATO *et al.* Proc. OFC'98 postdeadline paper PDP3, (San Jose, CA, 1998).